https://doi.org/10.5194/nhess-2024-184
Preprint. Discussion started: 2 December 2024

Natural Hazards and Earth System Sciences Discussions

Implementation of an interconnected fault system in PSHA, example on the Levant fault

Sarah El Kadri[1], Céline Beauval[1], Marlène Brax[2], Yann Klinger[3]

[1] Univ. Grenoble Alpes, Univ. Savoie Mont Blanc, CNRS, IRD, Univ. Gustave Eiffel, ISTerre, 38000 Grenoble, France
[2] National Council for Scientific Research, CNRS-L, P.O. Box 16-5432, Achrafyeh, 1100-2040 Beirut, Lebanon
[3] Université de Paris Cité, Institut de physique du globe de Paris, CNRS, 1, rue Jussieu, Paris, France

Correspondence to: Sarah El Kadri (sarahelkadry7@gmail.com)

Abstract.

The Levant Fault System (LFS), a 1200 km-long left-lateral strike-slip fault connecting the Red Sea to the East Anatolian fault, is a major source of seismic hazard in the Levant. In this study, we focus on improving regional Probabilistic Seismic Hazard Assessment (PSHA) models by considering the interconnected nature of the LFS, which challenges the traditional approach of treating faults as isolated segments. We analyze the segmentation of the fault system and identify 43 sections with lengths varying from 5 to 39 km along the main and secondary strands. Applying the SHERIFS (Seismic Hazard and Earthquake Rate In Fault Systems) algorithm, we develop an interconnected fault model that allows for complex ruptures, making assumptions on which sections can break together. At first, using a maximum magnitude of 7.5 for the system and considering that ruptures cannot pass major discontinuities, we compare the classical and interconnected fault models through the seismic rates and associated hazard results. We show that the interconnected fault model leads on average to increased hazard along the secondary faults, and lower hazard along the main strand, with respect to the classical implementation. Next, we show that in order for the maximum magnitude earthquake to be more realistic (~7.9), the connectivity of the LFS fault system must be fully released. At a 475-year return period, hazard levels obtained at the PGA are above 0.3g for all sites within ~20km of faults, with peak values around 0.5g along specific sections. At 0.2s spectral acceleration, hazard values exceed 0.8g along all fault segments. This study highlights the importance of incorporating complex fault interactions into seismic hazard models.

1 Introduction

The Levant Fault System (LFS) stretches approximately 1200 km from the Red Sea extensional fault system in the south to the East Anatolian fault system in the north, at the southern fault-rupture termination of the largest of the two 6 February 2023 Kharamanmaraş earthquakes (Zhang et al. 2023). The system is characterized by left-lateral strike-slip kinematics. Inside the Lebanese restraining bend, the fault splays into several branches: the Roum and Mount Lebanon faults to the west, Yammouneh, the main fault strand, in the center and the Rachaya and Serghaya faults to the east (Fig. 1a). The main strand accommodates most of the deformation with a mean slip rate ranging between 4 to 5 mm/yr (Daeron et al. 2004; Gomez et al. 2007a, b; Wechsler et al. 2018), whereas the secondary faults have slip rates estimated from 1 to 2 mm/yr (Gomez et al. 2003; Nemer and Meghraoui 2006, 2008).

Probabilistic Seismic Hazard Assessment (PSHA) is required to produce seismic hazard maps essential for establishing building codes (e.g. Meletti et al. 2021 in Italy; Danciu et al. 2024 within Europe; Sesetyan et al. 2018 in Turkey; or Wang et al. 2016 in Taiwan). In most of the source models built for PSHA, the conceptual representation of faults is rigid. Faults are made of a number of tectonically defined sections. Within a predefined

https://doi.org/10.5194/nhess-2024-184
Preprint. Discussion started: 2 December 2024

fault, ruptures can occur on individual sections or on a combination of sections. However, ruptures that would involve combination of sections from different predefined faults are not included in the model. The source models therefore usually include only a subset of the potential ruptures that may occur on the fault system.

El Kadri et al. (2023) published a seismic hazard model for Lebanon that integrates the major faults in the area in the classical way described above (Fig. 1a). Earthquake frequencies on these faults are inferred from a moment-balanced recurrence model relying on the geologic or geodetic mean slip rate evaluated for the fault. The source model also includes off-fault seismicity, through a catalog-based smoothed-seismicity model. El Kadri et al. (2023) follow the state-of-the-art standards in PSHA and deliver a distribution of seismic hazard levels for each site within Lebanon, which may be useful for future updates of the Lebanese building code. The present study aims to understand how the source model and eventually the hazard levels may change if an interconnected fault system is considered.

A number of earthquakes in the last 30 years have shown that ruptures can jump over some geometrical discontinuities, such as gaps or steps in the fault system, that were previously considered as major obstacles to rupture propagation. These jumps can result in larger magnitudes than anticipated (e.g., 2001 M_W 7.8 Kunlunshan earthquake in China, Klinger et al. 2005; 2010 M_W 7.2 El Mayor-Cucapah earthquake in Mexico, Fletcher et al. 2014; 2016 Kaikōura M_W7.8 in New Zealand, Klinger et al. 2018). Therefore, several methods have been developed to take into account these complex ruptures into hazard models. In 2014, the Working Group on California Earthquake Probabilities (WGCEP) developed a new inversion-based methodology called the "Grand inversion", to relax fault segmentation and incorporate multifault ruptures in the Uniform California Rupture Forecast (UCERF, Field et al., 2014; Page et al., 2014). Subsequently, Chartier et al. (2017) implemented the SHERIFS (Seismic Hazard and Earthquake Rate In Fault Systems) algorithm, a method to relax fault segmentation which is simpler than the UCERF framework and that requires less input parameters. Additional algorithms were also developed, such as the integer-programming optimization by Geist and ten Brink 2021, or the SUNFiSH approach by Visini et al. (2020). We focus on the SHERIFS algorithm, which has been applied on various crustal fault systems including the Corinth rift in Greece (Chartier et al. 2017), the North Anatolian Fault (Chartier et al. 2019), the Eastern Betics in southeastern Spain (Gomez Novell et al. 2020), the southeastern Tibetan Plateau (Cheng et al. 2021), faults in central Italy, (Moratto et al. 2023), and the Pallatanga–Puna fault in Ecuador (Harrichhausen et al., 2023).

Our aim is to build interconnected fault models for the Levant fault system, applying the algorithm SHERIFS, and to estimate the associated hazard levels. We consider the faults described in El Kadri et al. (2023), but rather than including them separately in the hazard calculation, we first go down to the section scale and then evaluate all possible section combinations, for all magnitudes up to the maximum magnitude earthquake. Our aim is to understand how the iterative process in the SHERIFS algorithm builds the set of ruptures and associated occurrence rates, and distributes the moment budget over the ruptures with the constraint that earthquake frequencies follow a given distribution at the scale of the system. We show that in order for the maximum magnitude earthquake to be realistic, the connectivity of the LFS fault system must be fully released. Finally, we derive probabilistic seismic hazard levels by combining our preferred fault model with a set of ground-motion models. To test our source model against observations, we compare the earthquake forecast with the available earthquake catalog at a regional scale, and with earthquake sequences observed in paleoseismic trenches at a local scale.

https://doi.org/10.5194/nhess-2024-184
Preprint. Discussion started: 2 December 2024

Natural Hazards and Earth System Sciences
Open Access
EGU
Discussions

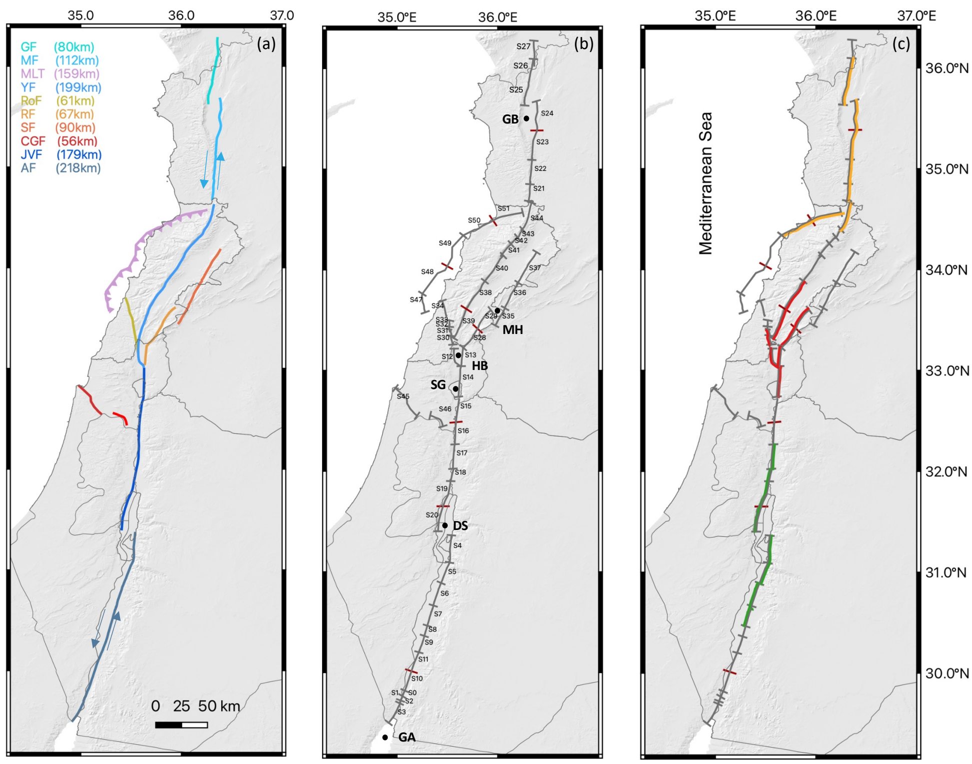

Figure 1 : The Levant Fault System. (a) Classical fault representation, the fault system is made of 10 main faults, GF: Ghab Fault, MF: Missyaf, MLT: Mount Lebanon thrust, YF: Yammouneh, RoF: Roum, RF: Rachaya, SF: Serghaya, CGF: Carmel-Gilboa, JVF: Jordan Valley, AF: Araba. (b) Detailed segmentation of the fault system, gray dash: tectonic discontinuities, red dash: arbitrary subdivision of sections required for homogenizing sections' length; GB: Ghab basin, MH: Mount Hermon, HB: Hula Basin, SG: Sea of Galilee, DS: Dead Sea, GA: Gulf of Aqaba. (c) Examples of possible complex ruptures that are not accounted for in the classical implementation of faults.

2 The Levant Fault System

The Levant Fault System (LFS) has been the source of multiple significant earthquakes (Fig. 2), resulting in extensive destruction, surface faulting, and alterations to the landscape. Lefevre et al. (2018) has summarized the known history of major earthquakes along the southern fault section, between the Gulf of Aqaba and the Sea of Galilée, over the last ~1200 years, based on tectonic, paleoseismic, and historical data. Brax et al. (2019) analyzed the literature on historical events in-between latitudes 31.5° and 35.5° (approximately from the Dead Sea to the Ghab pull-apart). A number of destructive earthquakes occurred, including the 363 earthquake (M~7.3) that may have ruptured sections on the Araba fault or both on the Araba and Jordan Valley fault (Ferry et al. 2011; Klinger et al. 2015), the 551 event (M~7.3) that probably ruptured the off-shore Mount Lebanon thrust (Elias et al. 2007), or the 1202 earthquake (M~7.6) that ruptured the Yammouneh fault (Daeron et al. 2007) as well a section of the Jordan Valley fault (Jordan Gorge fault, Wechsler et al. 2018). North of Lebanon, strong earthquakes have also occurred along the Missyaf and Ghab faults, in particular the 1170 and 1157 earthquake sequences (Meghraoui et al. 2003; Sbeinati et al. 2010).

To build the set of ruptures that may occur within the fault system, we need to move away from the regional-scale fault scheme of the LFS (Fig. 1a) and go down to the scale of the tectonic section. Several authors have studied the fault system and analyzed the segmentation. To the south, based on the location of major jogs and bends, Lefevre et al. (2018) proposed to split the Araba and Jordan Valley faults into 9 sections, up to the Hula Basin

https://doi.org/10.5194/nhess-2024-184
Preprint. Discussion started: 2 December 2024

segment south of Lebanon. Ferry et al. 2011 studied the Jordan Valley section, based on satellite photographs, field investigations, and offset measurements. They mapped in detail the fault trace in-between the Dead Sea and the Sea of Galilée and identified six 15 to 30km-long right-stepping sections limited by relay zones. Within the Lebanese restraining bend, Daeron (2005) mapped the Yammouneh fault based on satellite images, aerial photographs and topographic maps. Additionally, the Roum, Rachaya and Serghaya fault traces were mapped by Nemer and Meghraoui et al. (2006, 2008) through detailed field work and aerial-photograph analysis. Meghraoui (2015) discussed the LFS fault trace and its segmentation, from the Gulf of Aqaba to the Amik Basin in Turkey, identifying the geometrical complexities (large step overs, pull-apart basins, restraining bends) that may act as barriers to earthquake ruptures.

We have built on these studies and reanalyzed satellite images along the whole fault system, looking for distinct steps and bends to define the sections. We have carefully analyzed the geological features and incorporated the relevant local paleoseismic information. The LFS mostly exhibits transtensional features, such as the significant pull-apart structures of the Gulf of Aqaba, the Dead Sea (gap ~14km), and the Ghab pull-apart (~11km). Another major discontinuity is the compressional jog that forms Mount Hermon and separates the Rachaya and Serghaya faults (Fig. 1b). At a smaller scale, the LFS comprises linear strands characterized by left-lateral offsets of drainage systems, right-stepping ruptures exhibiting pressure and shutter ridges, and minor pull-apart basins distributed along its length (such as the Qalaat Al Hosn pull-apart basin at the Syrian/Lebanese border, the Hula Basin, or the Yammouneh basin along the Yammouneh fault). We have also observed push-up zones indicating uplift along the Araba Fault. In total, we obtained 43 sections with lengths varying from 5 to 39 km (Fig. 1b, Table 1). Future ruptures may break along one or several sections. For example, a large earthquake could start in the Dead Sea pull apart, and propagate bilaterally both to the south on the Araba fault and to the north on the Jordan Valley fault (Fig. 1c, green). A large earthquake could also involve a rupture on the main strand of Yammouneh fault together with ruptures on the Roum and Sergaya fault branches in the same event (Fig. 1c, red). This complexity needs to be included in order to make more realistic fault models for PSHA. The level of connectivity in the system depends on which discontinuities are considered firm barriers for earthquake ruptures.

Some faults might be mechanically independent, while others involve faults that interact with each other. The degree of fault interaction is related to the dynamics of the earthquake rupture process (Harris and Day 1993, Gupta and Scholz 2000). According to Scholz and Gupta (2000), the probability of an earthquake jumping from one fault to another increases with the degree of stress interactions between the faults. They introduced a criterion to estimate the degree of interaction based on separation and overlap of echelon normal faults, and recognized that the case of strike-slip faults is more complex. Wesnousky (2006) studied the mapped surface ruptures of 22 historical strike-slip earthquakes to understand the role of geometrical discontinuities in the propagation of earthquake ruptures, and to evaluate the possibility for predicting the endpoints of future earthquake ruptures. Based on this dataset, he showed that ruptures do not propagate across fault steps larger than 3-4 km. However, subsequent earthquakes, such as the 2010 M_W 7.2 El Mayor–Cucapah earthquake in Mexico (Fltecher et al. 2014) or the 2016 M_W 7.8 Kaikoura earthquake (Hamling et al. 2017), have challenged these conclusions and demonstrated that fault systems can undergo complex ruptures, involving numerous faults with various orientations and much larger stepovers. The Levant fault system includes significant discontinuities, with apparent step sizes exceeding 10 km (e.g. Ghab Basin, Mont Hermon, Dead Sea Basin). In the present work we test different levels of connectivity, allowing progressively larger jumps for ruptures. Nonetheless, it is important to keep in mind that within these discontinuities, substantial uncertainty exists regarding the presence of secondary faults connecting neighboring faults. Hence, these gaps might be smaller than they currently appear in map-view.

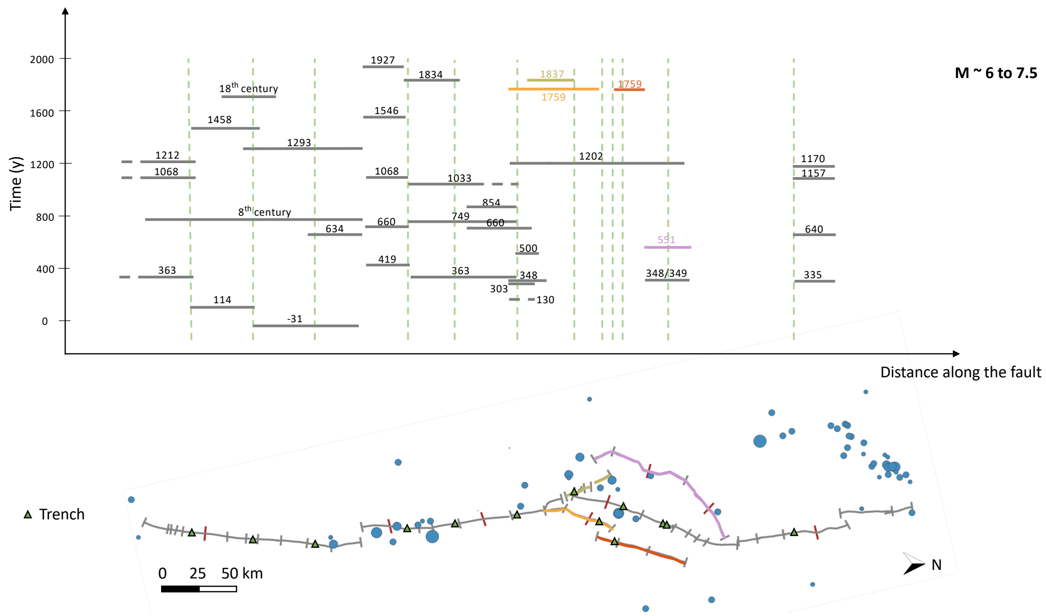

Figure 2 : Seismic activity in the region of the Levant Fault System. Top: paleoseismic events (horizontal bars, Lefevre et al. 2018) with extension of the ruptures inferred from observations in the trenches along the fault. Bottom: fault system with detailed segmentation, trenches (green triangles), instrumental events from global datasets (circles, magnitude larger or equal to 4.1, see Section 6), gray dash: tectonic discontinuities, red dash: arbitrary subdivision of sections.

3 SHERIFS iterative process

The SHERIFS algorithm (Chartier et al. 2017, 2019) aims at producing an interconnected fault model for PSHA by converting the moment rate stored within the fault system into earthquake rates along the faults. SHERIFS proposes a technique for distributing the moment rate budget over a number of earthquake ruptures within the system, with the constraint that earthquake rates follow a magnitude-frequency distribution at the level of the system. This magnitude-frequency distribution can be a Gutenberg-Richter distribution, or any other distribution (e.g. characteristic distribution). Ruptures can occur on sections alone or on combination of sections.

SHERIFS' algorithm delivers a set of sections and sections' combinations (ruptures) with associated magnitudes and occurrence rates. In previous applications of SHERIFS, no information is provided on the obtained distribution of rupture magnitudes in space. Knowing how seismic rates are distributed in space is key to understanding the geographical pattern of hazard levels. In PSHA, at a site, ground-motion exceedance rates are calculated by multiplying rates of ruptures with the probabilities that the ruptures produce an exceedance of the ground-motion levels at the site. Ruptures close to the site will contribute more than ruptures away from the site. In the present study, we aim at understanding the exact distribution in magnitude and space of the ruptures, and its link with hazard levels.

The algorithm requires as inputs:

- the set of fault sections' traces with extension at depth (dip angles and widths),
- the slip rates associated to every section,
- the geometrical rules for a section to be able to break with its neighboring sections: the maximum azimuth between two adjacent sections (here we use 75°) and the maximum distance between sections that a rupture may jump,

https://doi.org/10.5194/nhess-2024-184
Preprint. Discussion started: 2 December 2024

- an assumption on the shape of the magnitude-frequency distribution of the system (here we mainly use the Gutenberg-Richter distribution, but a characteristic distribution could also be considered),
- the selection of a scaling relationship to associate magnitudes to rupture area, here we use Leonard 2014 equations for interplate earthquakes,
- an estimate for the maximum earthquake magnitude within the system.

If the length of the sections is too heterogeneous, the algorithm subdivides the longest sections into shorter sections to homogenize sections' length. Within the Levant fault system, nine tectonic sections are arbitrarily subdivided into two sections, resulting in 52 sections in total within the fault system (Fig. 1b). Table 1 summarizes the characteristics of the sections considered. References for the mean slip rates can be found in El Kadri et al. (2023).

Based on the hypothesis that earthquake rates follow a Gutenberg-Richter distribution, a probability density function (PDF) for the magnitude is built, corresponding to the relative contribution of the magnitude bins in terms of moment rates within the system (Fig. 3, see also Chartier et al. 2017, 2019). The exponential decrease of rates with increasing magnitudes is compensated by the huge increase in moment rate with magnitude. Using this pdf to sample magnitudes, large magnitudes are picked much more frequently than low magnitudes.

The moment rate is distributed through an iterative process over magnitudes and associated sections or sections combinations. In a preliminary step, the algorithm establishes all possible ruptures, or section combinations, and associates earthquake magnitudes to these ruptures by applying the area-magnitude scaling relationship. Then, an iterative process starts (Figure 3) where at each iteration, the same amount of slip rate is spent (called 'dsr'). This process is as follows:
1) A magnitude is randomly picked in the pdf.
2) A rupture is selected randomly from the pool of ruptures with areas matching the magnitude, according to the scaling relationship.
3) The moment rate spent in the iteration is calculated based on the total area of the rupture, the shear modulus and the slip rate increment (Fig. 3).
4) The seismic rate is eventually obtained dividing this moment rate by the moment corresponding to the magnitude.

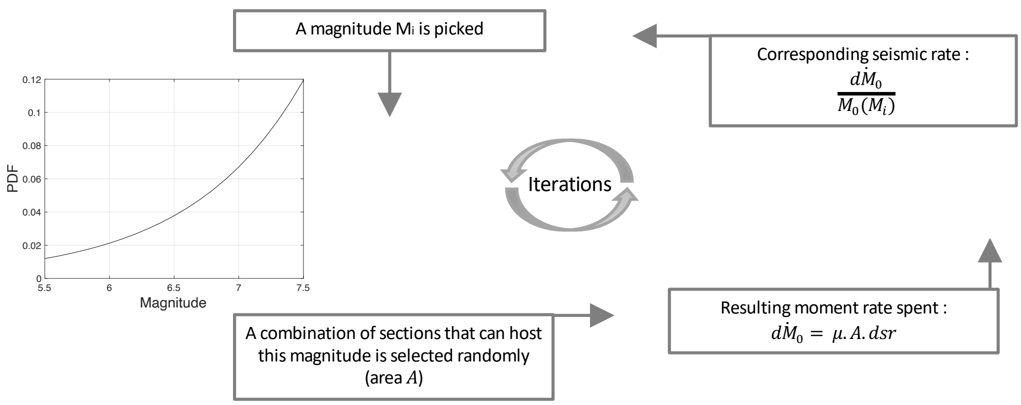

Figure 3: Scheme illustrating the main steps of the SHERIFS iterative process where an amount of slip rate 'dsr' must be spent: 1) a magnitude M_i is picked; 2) a combination of one or several sections that can host this magnitude is selected; 3) the associated moment rate is estimated considering the slip rate increment, the area of the rupture A and the shear modulus μ; 4) the seismic rate is estimated dividing the moment rate by the moment M_o corresponding to this magnitude. The iterative process goes on until the sum of all section slip rates is exhausted. PDF to sample the magnitude established considering a Gutenberg-Richter with b-value=1 and M_{max}=7.5.

Each time a section participates in a rupture, its slip rate budget decreases accordingly. When a section has no slip rate left, it cannot participate in any new ruptures. The iterative process goes on until the slip rate of all sections in the system is exhausted. Our tests show that the increment in slip rate must be very small to ensure a homogeneous distribution of seismic rates over the system (here we use 0.0001 mm/year).

Large magnitudes are picked more frequently than low magnitudes, so the upper range of the system-level magnitude-frequency distribution is first built, then the remaining moment rate budget is spent over lower magnitudes until no budget is left. During the iterative process, at some point the rates of the largest magnitudes stabilize because some sections required to create these large ruptures have their slip rate exhausted. The shape of the magnitude-frequency distribution is anchored to the rates in the upper-magnitude range (see Chartier et al. 2017, 2019). As will be shown in the application on the Levant fault system, understanding the role of these "anchor points" is key to fully grasp how the SHERIFS algorithm works and why the moment rate budget can never be spent entirely.

4 First application on the Levant fault system and comparison with the classical implementation

We start with a test that enables the comparison with the classical implementation of faults (Figure 1a). We consider that ruptures cannot jump major discontinuities (Ghab pull-apart, Dead Sea pull-apart, Mount Hermon jog, gap between Roum and Mount Lebanon Fault), therefore we set the maximum jump to 10km. All sections can break with their neighbors, except those separated by these four gaps. We consider a maximum magnitude of 7.5 in the system, corresponding to the maximum magnitude earthquake in the classical implementation of faults, using the mean rupture area predicted by the Leonard (2014) scaling relationship (maximum length ~200km and width 18km, Yammouneh, Jordan Valley, and Araba faults, Fig. 1a).

4.1 Iterative process, the system magnitude-frequency distribution (MFD) and the anchor points

Using a slip rate increment of 0.0001 mm/yr, in total ~1.9 million iterations are required to spend the system slip-rate budget. Figure 4 illustrates the process at three different steps. The first column displays, for the iteration n°1500, the moment rate already spent per magnitude interval (Fig. 4a, in blue), earthquake rates distributed within the system (Fig. 4b, in blue), and the fault sections that still have some budget to spend at this stage (in grey, all of them). The second column provides an update at iteration n°786300, with the moment rate spent and magnitude rates in orange. At that iteration, the rates in the upper magnitude range (i.e. 7.3-7.5) are fixed and the Gutenberg-Richter MFD of the system is anchored to these upper magnitude rates (black straight line). A number of sections have spent entirely their budget (Fig. 4f, in orange), others still have some budget (in grey), but no more large magnitudes (7.3-7.5) can be produced. In subsequent iterations, magnitudes continue to be sampled in the PDF and the remaining slip rate budget is spent until the seismic rates reach the system MFD (Fig. 4h, green crosses align with the black line). Any slip rate increment that leads to higher rates than predicted in a magnitude bin is discarded and considered aseismic slip. The third column displays results at the final iteration: the total moment rate spent (in green), the final magnitude-frequency distribution (in green), and the sections that have either consumed entirely their budget (orange and green), or have part of their slip budget converted into aseismic deformation (in grey). Overall, in this calculation, 9% of the slip rate budget was not spent on earthquakes. Chartier et al. (2017) call the unused slip rate 'non-mainshock slip'. We prefer to simply state that part of the slip rate is not used and is considered aseismic slip. This aseismic slip may correspond to creep or afterslip of major events. Chartier et al. (2019) uses this unused slip rate as an indicator of whether the model is reasonable or not. Most studies consider that the slip rate deficit along the Levant fault system will be entirely released in earthquakes and that creep is negligible (Gomez et al. 2003, Daeron et al. 2004, Gomez et al. 2007b, Wechsler et al. 2018), so 9% is an acceptable amount of aseismic deformation.

https://doi.org/10.5194/nhess-2024-184
Preprint. Discussion started: 2 December 2024

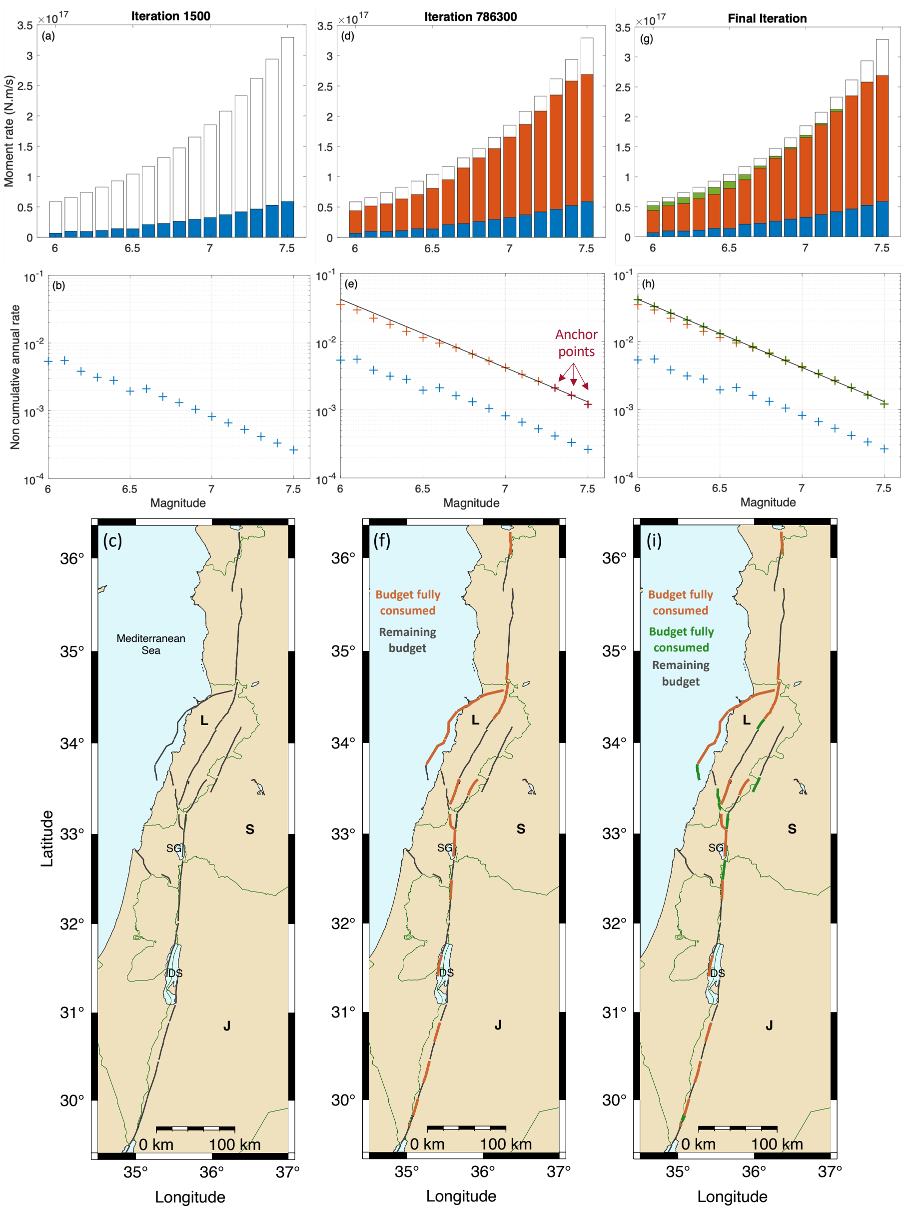

Figure 3 : Illustration of the iterative process in SHERIFS, at 2 intermediary steps (1st and 2nd column) and final step (3rd column). Maximum magnitude within the system 7.5 and maximum jump 10km. First row: in color, moment rate spent per magnitude bin (white: total budget available). Second row: seismic rates distributed over the fault system. Third row: fault sections that still have some budget to spent (gray), sections with slip budget exhausted (orange, then green), in (i) : end of the process, sections with part of the slip budget converted into aseismic slip (grey). See the text. L: Lebanon, S:Syria, J:Jordan, SG: Sea of Galilee, DS: Dead Sea

https://doi.org/10.5194/nhess-2024-184
Preprint. Discussion started: 2 December 2024

4.2 The distribution of magnitude rates in space

As in any probabilistic seismic hazard study, we need to know where the seismic rates are distributed in space and in magnitude. With SHERIFS, because the moment rate (or slip rate) is distributed in a huge number of ruptures (combination of sections), it is not straightforward to display this information. One solution is to estimate the participation rate of the sections to given magnitude earthquakes. Figure 5 displays the annual rates of occurrence obtained for its participation to magnitude M_w6, M_w6.5 and M_w7.5 ruptures, respectively, for every section of the fault system. Rates are normalized by the section area in order to be comparable throughout the system. We run several times the SHERIFS algorithm and the distribution of the magnitude rates in space results very similar. Figure 5 shows that whatever the magnitude, the distribution of earthquake ruptures along the system are not homogeneous and rates vary strongly between sections. For magnitudes 6 and 6.5, the highest rates (orange to red) are obtained on the southern half of the Yammouneh fault, southern sections of Jordan Valley fault, and northern sections of Araba Fault. For magnitudes 7.5, we observe the opposite, the highest rates are obtained along the northern part of the JVF, and along the northern sections of the Yammouneh fault. Owing to the shape of the probability density function, SHERIFS algorithm is more likely to pick magnitudes in the upper magnitude range than in the lower magnitude range. Sections that participate in large magnitude ruptures have less slip rate available for moderate magnitude ruptures. Note that because for now ruptures are not allowed to jump gaps larger than 10km, the sections north of Ghab pull-apart, as well as on the Sergaya fault, cannot participate to a magnitude 7.5 (in grey in Fig. 5c).

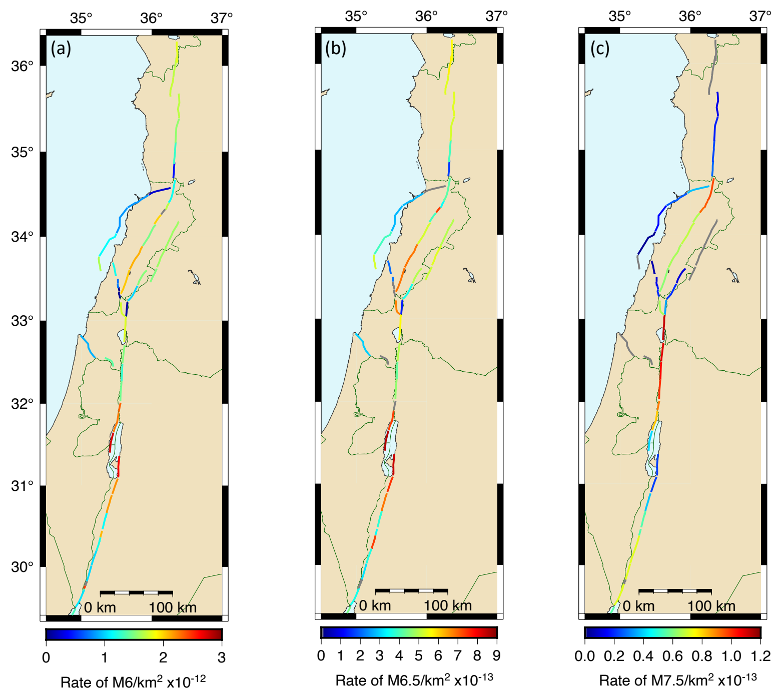

Figure 5 : Annual rates of earthquakes for magnitudes M_w 6, 6.5, and 7.5, normalized per square kilometer for each segment of the fault system.

4.3 Earthquake rates forecast: interconnected versus classical approach

The moment budget available for earthquakes relies on the slip rates of fault sections and is the same as in the classical implementation of faults. However, the distribution of this moment budget over earthquake ruptures is not similar, as the interconnected fault model includes much more rupture possibilities between sections than the classical implementation. In the interconnected fault model (with maximum jump 10km), ruptures can combine sections from both the Missyaf and Yammouneh faults, or sections from both the Missyaf and Mount Lebanon fault. Also, sections that belong to the Roum fault can break with sections on Yammouneh, Rachaya, and/or the Jordan Valley faults. In figure 4a, we compare the fault-system MFD obtained with SHERIFS with the fault-system MFD that corresponds to the classical implementation (i.e. the sum of individual Gutenberg-Richter MFDs). We observe that earthquake rates corresponding to the interconnected model are slightly lower in the moderate magnitude range, and slightly higher in the upper magnitude range close to M_{max}. This can be understood by highlighting the sections that can participate in the maximum magnitude M_{max} ruptures (Figs. 4b and 4c, in blue): more sections can participate in a magnitude 7.5 earthquake in the interconnected model than in the classical (rigid) implementation. There is more moment rate available for the upper-magnitude range, as the model is moment-balanced there is slightly less moment rate available for earthquakes in the moderate-magnitude range.

When performing the comparison at the level of the named faults defined in Fig. 1 (e.g., Yammouneh, Rachaya, etc…), the differences obtained between the classical and the interconnected approach are much larger. Figure 7 displays the magnitude-frequency distributions in the classical implementation of faults, superimposed to the participation rates obtained in the interconnected fault model. The sections involved are the same, but in the case of the interconnected fault model, the sections can participate in larger ruptures that include sections from neighboring faults. For example, sections of the Rachaya fault are limited to magnitude 7.1 ruptures in the classical implementation; whereas in the interconnected model they can participate in ruptures up to 7.5. As the moment rate budget is the same, the rates in the moderate magnitude range are lower in the interconnected fault model, with respect to the classical fault model.

https://doi.org/10.5194/nhess-2024-184
Preprint. Discussion started: 2 December 2024

Natural Hazards and Earth System Sciences
Open Access
Discussions

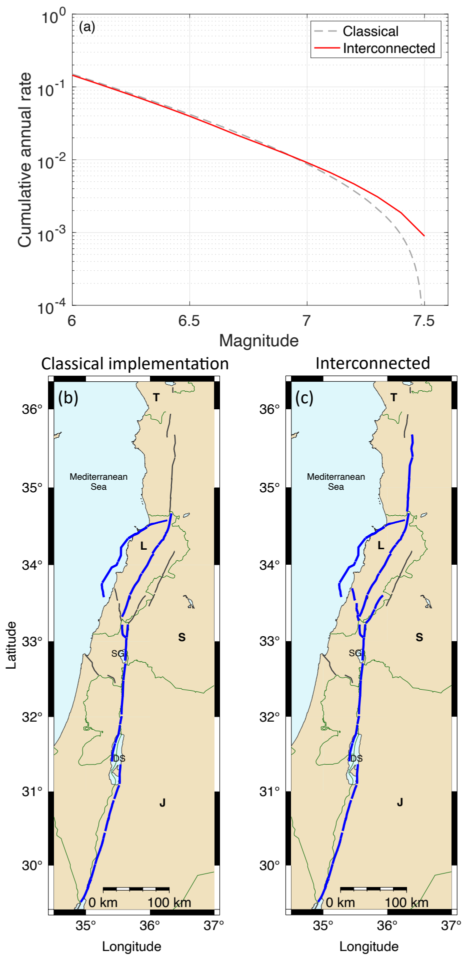

Figure 4 : Comparison between the classical implementation of faults, and the interconnected model. (a) Magnitude-frequency distributions at the scale of the whole fault system (assumption M_{max} 7.5), both distributions are moment-balanced using the fault slip rate. (b) Classical and (c) Interconnected fault model, in blue sections that can participate in a maximum magnitude M_{max} 7.5 rupture. More sections can participate in the interconnected fault model, so more moment rate is available for the upper magnitude range.

https://doi.org/10.5194/nhess-2024-184
Preprint. Discussion started: 2 December 2024

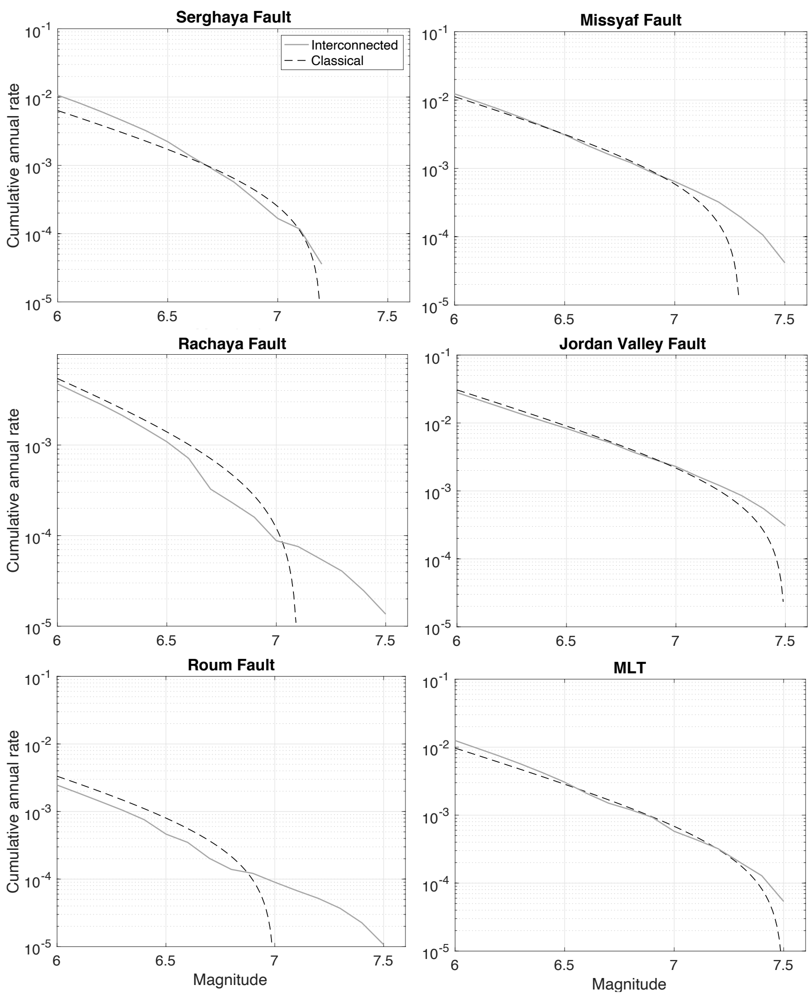

Figure 7: Magnitude-frequency distributions for 6 example faults in the classical implementation (dashed lines), compared to participation rates obtained with SHERIFS (solid lines). Assumption M_{max} 7.5. Interconnected model with maximum jump 10km. Participation rates: seismic rates associated to the segments are summed, some ruptures may involve sections that do not belong to the fault.

4.4 Hazard levels at 475 years – interconnected versus classical approach

To compare the classical and interconnected fault models in terms of hazard level, we ran two hazard calculations that combine the same set of ground-motion models respectively with the two different fault models. Two seismic hazard maps for the PGA at 475 years return period were produced (Fig. 8, generic rock site with V_{S30} = 760 m/s). Following El Kadri et al. (2023), we include three ground-motion models equally weighted in a logic tree: Chiou and Youngs (2014), Akkar et al. (2014) and Kotha et al. (2020). The three models predict ground motions for shallow crustal earthquakes. Hazard calculations are performed with the Openquake engine (Pagani et al. 2014). We truncated the gaussian distribution at 3 standard deviations above the mean.

Both seismic hazard maps display Peak Ground Accelerations (PGAs) of 0.7-0.8g for a mean return period of 475 years, but there are major differences in the hazard patterns obtained. In the classical implementation, the hazard is much higher (up to 0.7-0.8g) along the more rapid main strand than on the slower secondary faults (up to 0.4-

https://doi.org/10.5194/nhess-2024-184
Preprint. Discussion started: 2 December 2024

Natural Hazards and Earth System Sciences
Discussions

0.5g); whereas in the interconnected fault model, secondary faults may pose a comparable threat as the main strand. Overall, using the interconnected fault model, the hazard levels decrease along the main strand (from ~0.7-0.8 to ~0.5-0.6g), but increase along the secondary faults (from ~0.4 to ~0.5g), with respect to the classical implementation. In the interconnected model, hazard levels are no longer uniform within a fault, they vary significantly depending on the location of the site along the fault. They are highest along the southern part of the Yammouneh fault, as well as along the southern part of JVF, and northern part of Araba fault, corresponding to the sections with the highest rates in the moderate magnitude range (Figs. 5a and 5b, rates for magnitudes 6 and 6.5). These higher hazard levels can be explained by the observation that moderate magnitudes often control hazard estimates at 475 years return period, when a Gutenberg-Richter model is used (e.g., El Kadri et al. 2023).

For sites above the dipping Mount Lebanon Thrust, the interconnected fault model delivers hazard levels much higher along the southern part than in the north. The northern sections of Mount Lebanon Thrust are involved in more large magnitude ruptures than the southern sections, as they may break with segments from the Missyaf and Yammouneh faults. Southern sections cannot rupture with the Roum fault when the maximum jump is set to 10km and as a consequence, annual rates of moderate magnitudes are higher in the south resulting in higher hazard.

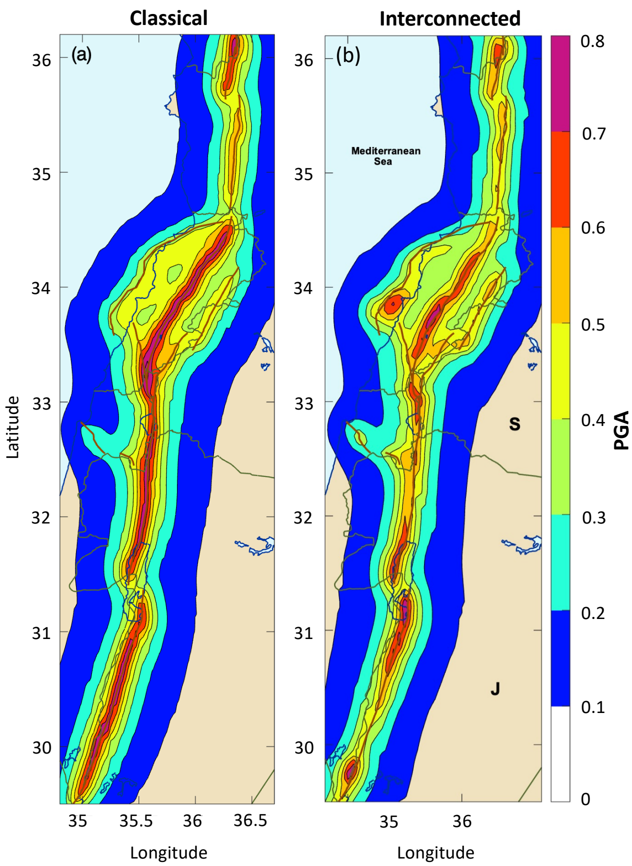

Figure 8 : Seismic hazard maps, PGAs at a 475 year return period (a) based on the classical implementation of faults, assuming that the maximum magnitude is M_{max} 7.5, (b) based on the interconnected model assuming M_{max} 7.5 (maximum jump 10km, ruptures cannot jump major discontinuities). Generic rock site condition (V_{S30}=760 m/s).

5 A realistic fault model for the Levant fault system: full connectivity and M_{max} 7.9

https://doi.org/10.5194/nhess-2024-184
Preprint. Discussion started: 2 December 2024

Natural Hazards and Earth System Sciences Open Access Discussions EGU

Reviewing other major strike-slip fault systems worldwide and the largest earthquakes they have generated (e.g. the M_W 7.8 1906 earthquake on the San Andreas, Yeats et al. 1997; 2002 M_W 7.9 Earthquake along the Denali fault in Alaska, Eberhart-Phillips et al. 2003; or the recent 2023 M_W 7.8 earthquake on the East Anatolian fault, Zhang et al. 2023), we believe magnitudes larger than 7.5 could occur along the Levant fault system. Thus, the source model for PSHA must include the possibility for large events, and therefore we test two potential maximum magnitudes: 7.9 and 8.1.

5.1 Test with M_{max} 7.9 and need for full connectivity

To begin with, we run the algorithm with a maximum magnitude of 7.9, keeping all other parameters as in Section 4. In particular, we start with a maximum jump of 10km. Sections on the Araba, Serghaya and Ghab faults cannot participate in a magnitude 7.9 rupture (Fig. 9a, sections in blue). Many sections are left with more than 50% of the slip rate not used (Fig. 9b, sections in orange). Sixty-four percent of the total slip rate is not spent on earthquakes (Fig. 9b). Such a high percentage of aseismic slip is not realistic in the light of what is known for the LFS. Next, we increase the maximum jump for ruptures from 10 to 12 km and run a new calculation so that ruptures can jump over the Ghab pull-apart as well as over Mount Hermon jog (Fig. 9c). All sections can now participate in a magnitude 7.9 earthquake, except for sections on the Araba fault. Only a few end-fault segments are left with more than half of the slip rate unused (Fig. 9d). In this run, twenty one percent of the total slip rate is not spent on earthquakes.

Lastly, we increase the maximum jump to 18km so that the fault system is now entirely connected and ruptures can jump over all major discontinuities, including the gap between Roum and Mount Lebanon fault (Fig. 9e). All sections can participate in a magnitude 7.9 rupture. In this case, the interconnected fault model uses 95% of the slip rate budget, with 5% of the budget considered aseismic slip. This low fraction of aseismic slip is compatible with the studies showing that this fault system is nearly entirely coupled (e.g., Wechsler et al. 2018, al Tarazi et al. 2011).

Figure 10 displays the distribution of the moment rate spent in earthquakes as well as the fault-system MFDs obtained for the three different runs. Increasing the connectivity from a 10km maximum jump (light grey histogram) to a 12km maximum jump (dark grey histogram) or a 18km maximum jump with full connectivity (black histogram), the moment rate spent in earthquakes increases. When full connectivity is applied, the moment rate spent (dark histogram) is close to the total moment rate stored in the system (white histogram). When ruptures cannot jump over major discontinuities (Fig. 9a), only a fraction of the sections can participate in the maximum magnitude earthquakes. Thus, rates for earthquakes in the upper magnitude range are low (Fig. 10b, light grey crosses). These rates constitute the anchor points of the system MFD and thus limit the rates over the whole system (light grey dash-dotted curve). Increasing connectivity, more sections can participate in the maximum magnitude earthquakes, the system MFD is anchored on higher rates, and more moment rate can be spent into earthquakes within the whole magnitude range (dashed dark grey curve for 12km jump, dark solid curve for full connectivity, Fig. 10b).

5.2 Selection of the most realistic model among models tested

In our last test, we kept a fault system entirely connected and increased the maximum magnitude to 8.1. Figure 11 summarizes the tests achieved and displays the system MFD resulting from:

- a run with M_{max} 7.5 and major discontinuities acting as barriers (Section 4)
- a run with M_{max} 7.9 and a fully connected system,
- a run with M_{max} 8.1 and a fully connected system.

The moment rate available for earthquakes within the system is constant (proportional to the slip rates and section surfaces), therefore when increasing the maximum magnitude of the Gutenberg-Richter model, the rates of moderate magnitude earthquakes decrease. Earthquakes with magnitude close to 8.0 are believed to have

https://doi.org/10.5194/nhess-2024-184
Preprint. Discussion started: 2 December 2024

Natural Hazards and Earth System Sciences
Open Access
EGU
Discussions

possibly occurred in the past along the Levant fault system (e.g. Lu et al. 2020). We believe that a 5% percentage of aseismic deformation is more realistic than 9 or 11%, for the Levant fault system. Therefore, the fully interconnected fault model with maximum magnitude earthquake 7.9 is our preferred model. Next, we calculate the hazard levels obtained when combining this fault model with a set of ground-motion models.

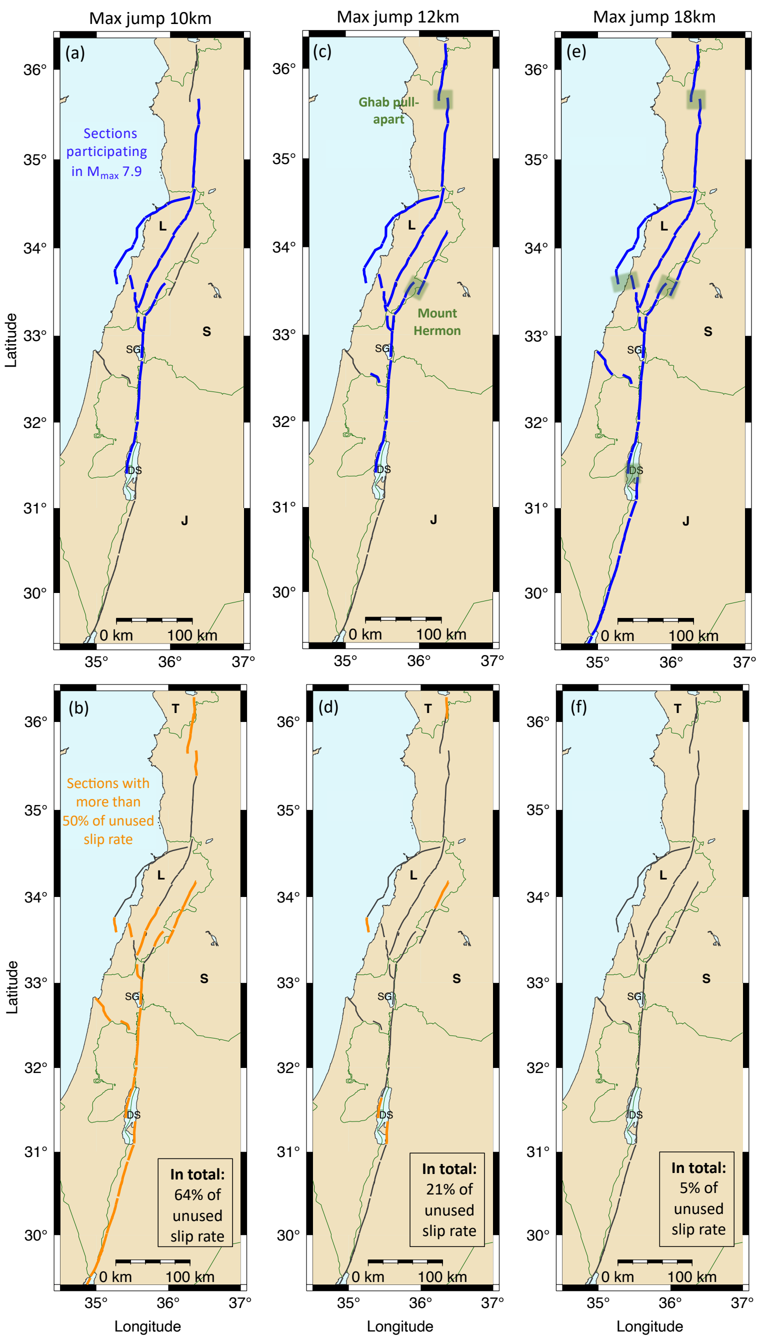

https://doi.org/10.5194/nhess-2024-184
Preprint. Discussion started: 2 December 2024

Figure 9: Increasing the connectivity in a fault model with M_{max} 7.9. 1st column: jump up to 10km allowed, 2nd column: jump up to 12km (ruptures can pass through Ghab pull apart and Mount Hermon jog), 3rd column: jump up to 18km (entirely connected, ruptures can pass all major discontinuities). 1st row, blue: sections that can participate in a M_{max} 7.9 rupture, green: discontinuities that ruptures can pass. 2nd row, orange: sections left with more than 50% unused slip rate at the end of the run; the percentage of the slip rate not used at the scale of the fault system is indicated.

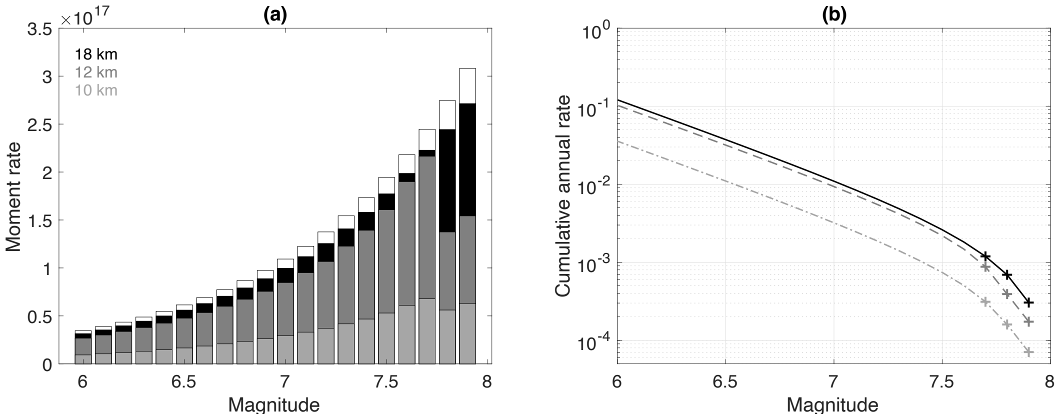

Figure 10: Increasing the connectivity in a fault model with M_{max} 7.9, (a) distribution of the moment rate spent per magnitude bin and (b) magnitude-frequency distribution, at the scale of the fault system. Light grey: ruptures cannot jump more than 10km (Fig. 9a), dark grey: maximum jump for ruptures of 12km (Fig. 9c), black: maximum jump 18km, system is entirely connected (Fig. 9e).

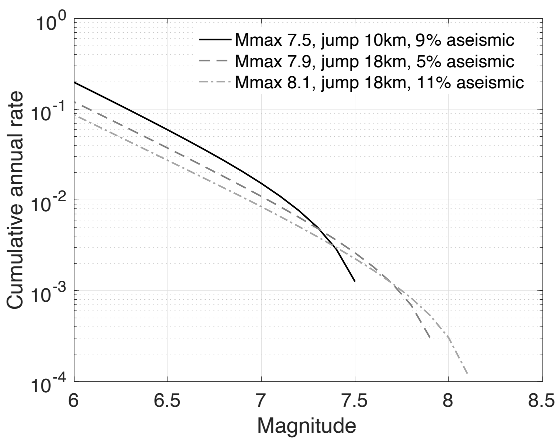

Figure 11: (a) Magnitude-frequency distribution obtained at the scale of the fault system, for three runs of SHERIFs. Solid curve: assumption M_{max} 7.5 and the major discontinuities act as barriers (Section 4). Dashed curve: assumption M_{max} 7.9 and the system is entirely connected. Dashed-dot curve: assumption M_{max} 8.1 and the system is entirely connected. All models are moment-balanced, but the percentage of unused slip rate varies with the model (respectively 9, 5 and 11%). Our preferred model is the fully interconnected model with M_{max} 7.9 (see the text).

5.3 Hazard levels associated to our preferred fault model (M_{max} 7.9 and full connectivity)

Figure 12 displays the seismic hazard map obtained for the PGA and 0.2s spectral acceleration at 475 years return period, by combining the M_{max} 7.9 interconnected model with the ground-motion logic tree. As expected, the PGA levels at 475 years return period are lower than obtained from the model with M_{max} 7.5 (Fig. 8b), due to the decrease of seismic rates in the moderate magnitude range (Fig. 11). At all sites within ~20km of the faults, PGA

https://doi.org/10.5194/nhess-2024-184
Preprint. Discussion started: 2 December 2024

Natural Hazards and Earth System Sciences
Open Access
Discussions

values are above 0.3g, except on the northern part of Mount Lebanon fault inland. PGA values are larger than 0.4g at most sites along the Ghab fault, Yammouneh fault, the southern part of Mount Lebanon fault, the central part of Jordan Valley fault, and the Araba fault. Peak values above 0.5g are found mainly at sites along the southern sections of the Mount Lebanon fault, as well as to the north and to the south of the Araba fault. These peak values are likely due to higher rates of moderate magnitudes on these sections. Figure 12b displays spectral accelerations at 0.2s for the same return period 475 years.

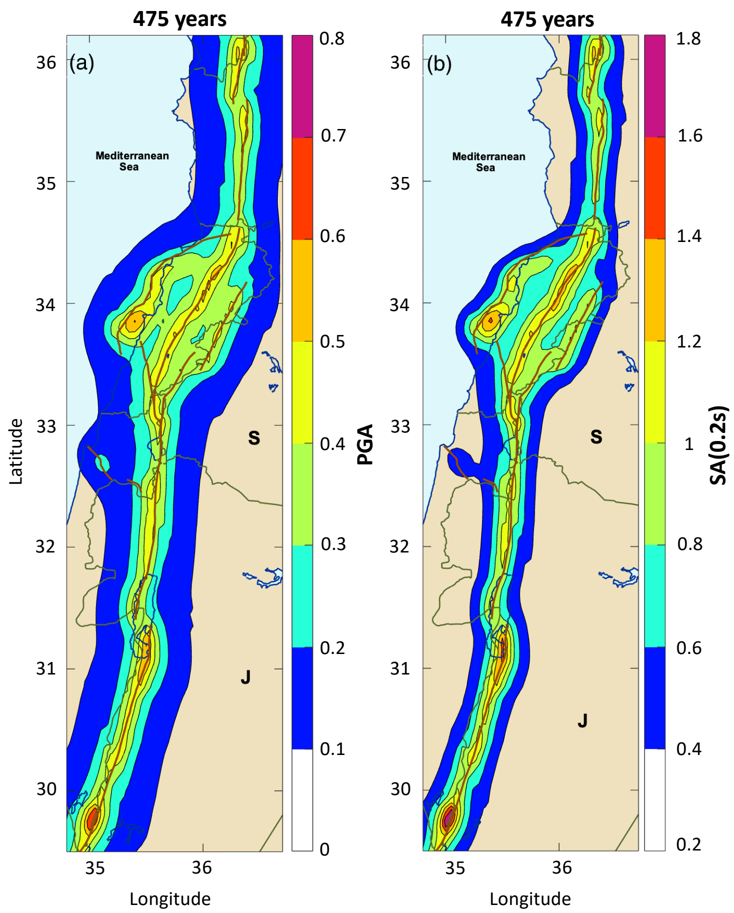

Figure 12: Seismic hazard map for a return period of 475 years based on a fully interconnected model assuming M_{max} 7.9. (a) at the PGA, (b) at 0.2s spectral acceleration. Generic rock site condition (V_{S30}=760 m/s).

6 Comparison of the modeled rates with the available observations

The fault model built for PSHA is made of earthquake ruptures and associated annual rates of occurrence. The earthquake forecast delivers a magnitude-frequency distribution at the scale of the fault system that follows a given shape. Both the earthquake catalog of the region and the available paleoseismic data were not used to derive the model; these observations can be compared with the earthquake forecast.

https://doi.org/10.5194/nhess-2024-184
Preprint. Discussion started: 2 December 2024

6.1 Observed earthquake rates for the region

Our model forecasts earthquakes on the fault system and at this stage no background seismicity is added. We build an earthquake catalog for the region keeping in mind that only the largest magnitudes may be associated with the main faults.

Brax et al. (2019) published a catalog of historical earthquakes for the Lebanese region between latitudes 31.5° and 35.5°. For every earthquake, the authors evaluated the information available in historical accounts, as well as the macroseismic intensity datasets produced and their interpretations in terms of epicentral location and magnitude estimate. Earthquakes whose existence is attested, but for which it was not possible to find a solution relying on clearly identified historical sources and intensity data have not been included (see Electronic Supplement 2 in Brax et al. 2019). For the period before 1900, we used the Brax et al. (2019) catalog, supplemented south of latitude 31.5° and north of latitude 35.5° by earthquake solutions from the EMME earthquake catalog (Zare et al. 2014), resulting in 23 earthquakes in total (Fig. 2 and Fig. 13).

We used global instrumental catalogs over the period 1900 to 2020, within the spatial window 34.5° to 37° in longitude, and 29° to 37° in latitude. We consider the ISC-GEM (International Seismological Center - Global Earthquake Model, Version 10, Storchak et al., 2015), GCMT (Global Centroid Moment Tensors, Ekström et al., 2012) and ISC (International Seismological Centre, Storchak et al. 2020) catalogs. From the ISC catalog we include only earthquakes with an ISC location and a magnitude M_S or m_b (that we convert into M_w applying equations from Lolli et al. 2014). We obtain 35 instrumental events with magnitude M_w ranging from 4.1 to 6.1.

Figure 13 displays the earthquake catalog obtained: destructive earthquakes with magnitudes larger or equal to ~6.5 occurred regularly in the last 2000 years in the region. The last one within this spatial window struck southern Lebanon in 1837. Magnitudes of historical earthquakes bear large uncertainties (see e.g. Brax et al. 2019), nonetheless such high magnitude levels are confirmed by the analysis of numerous paleoseismic trenches available along the LFS. The distribution of magnitudes in the interval 5.5-6.5 is particularly irregular over time. In the instrumental period starting in 1900, the largest earthquake in the spatial window is the M_w6.1 1927 Jericho earthquake (magnitude from the ISC-GEM catalog). The instrumental catalog also bears significant uncertainties as only global data have been included. Brax et al. (2019) did include earthquake solutions from local networks in the region. Different magnitude types are provided and to merge the datasets, several conversions between magnitudes are required (see Electronic Supplement 3 in Brax et al. 2019). The dispersion observed in the magnitude comparisons is very large in most cases. In this study, we prefer to use only global catalogs and ensure a certain level of homogeneity in the magnitude estimate, at the cost of a higher magnitude of completeness.

Earthquake rates are estimated considering a magnitude interval of 0.5. Based on cumulative number of events versus time plots, we evaluate that magnitudes larger or equal to 7.1 are complete since 363, magnitudes larger or equal to 6.6 since 1170, magnitudes larger or equal to 4.6 since 1981, and larger or equal to 4.1 since 2003 (Fig. 13). For the magnitude interval 5.6-6.6, there are too few earthquakes to estimate the period of completeness. We estimate periods from the ISC-GEM catalog at the global scale: magnitudes larger or equal to 5.6 are considered complete since 1965, and magnitudes larger or equal to 6.1 since 1925. Additionally, to get a rough estimation of the impact of magnitude uncertainties on rates, we generated 100 synthetic catalogs from the original one, sampling the magnitude of each earthquake from a gaussian distribution centered on the original magnitude with a standard deviation of 0.3 for historical events and 0.1 for instrumental events.

Cumulative annual rates are displayed in Fig. 14, superimposed to the modeled magnitude-frequency distribution for the fault system (our preferred model with M_{max} 7.9 in orange). The rate estimates from an analysis of paleoseismic trenches are also superimposed (Lefevre et al. 2018). We assume that all events with magnitude larger or equal to 7.1 and most events with magnitude larger or equal to 6.1 occurred on a fault. The model is roughly consistent with observations for magnitudes larger or equal to 6.6, but forecasts more events than observed for magnitudes larger or equal to 6.1. Up to now we have tested only the Gutenberg-Richter exponential distribution for the system. To know if a characteristic Youngs and Coppersmith (1985) distribution would be more compatible with observed rates, we run again the algorithm with an M_{max} 7.9, full connectivity, and a

https://doi.org/10.5194/nhess-2024-184
Preprint. Discussion started: 2 December 2024

Natural Hazards and Earth System Sciences
Open Access
EGU
Discussions

characteristic earthquake model. The model obtained is roughly consistent for magnitudes larger or equal to 7.1, but strongly underpredicts rates for magnitudes larger or equal to 6.6 and 6.1. Fourteen percent of the total slip rate is not used and considered aseismic, which is not realistic.

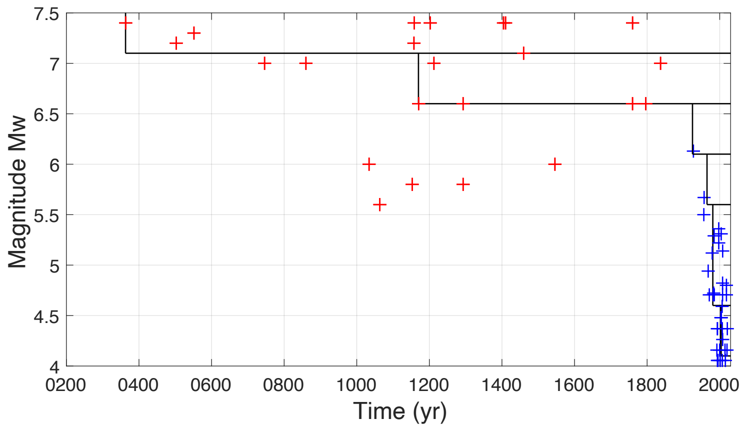

Figure 13: Earthquake catalog used (same as in Fig. 2), magnitude versus time, historical (red) and instrumental (blue) events. Periods of completeness per magnitude interval are indicated (straight lines).

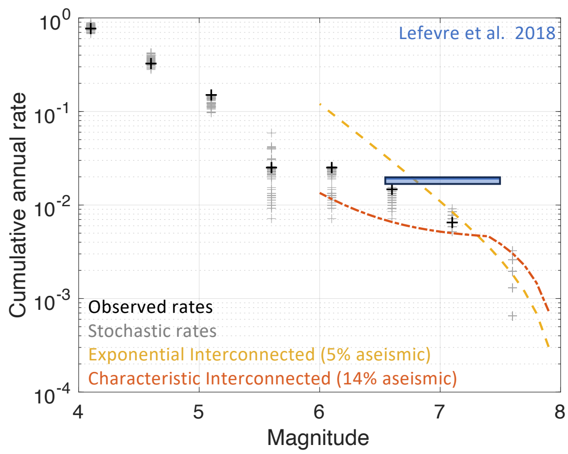

Figure 14: Magnitude-frequency distributions compared to observed rates. Black crosses: observed annual rates estimated from the regional earthquake catalog, grey crosses: annual rates from synthetic earthquake catalogs to account for uncertainties on magnitudes. Orange dashed curve: fault system MFDs, assumption Gutenberg-Richter, model with M_{max} 7.9. Red dashed curve: fault system MFDs, assumption characteristic model Youngs and Coppersmith with M_{max} 7.9.

6.2 Earthquake rates from paleoseismic trenches

Paleoseismic studies provide information on earthquakes that occurred before historical times and thus extend the observation time window available. Several trenches have been excavated along the Levant Fault System. They deliver key data on the size and on the timing of the earthquakes that ruptured the fault at the trench site. From the fault model built with SHERIFS, we can extract the set of ruptures passing through the trench site, with associated rates, and compare this forecast with the paleoseismic data.

https://doi.org/10.5194/nhess-2024-184
Preprint. Discussion started: 2 December 2024

Daeron et al. (2007) analyzed in detail a trench across the Yammouneh basin. They identified ten to thirteen paleo-events extending back more than ~12kyr, and they were able to provide reliable age bounds for half of these events. In the historical period, the most recent event is the 1202 destructive earthquake (magnitude estimate 7–7.8, according to Ambraseys and Jackson, 1998). They also identified an earthquake that occurred between 30 B.C. and A.D. 469. We consider these two earthquakes in the historical period, as well as 6 prehistoric earthquakes that occurred in a period extending over ~5600 years starting ~12kyrs ago (record considered complete over the period, events S7 to S12, see Daeron et al. 2007). Estimates for six inter-event times are thus available. To take into account the uncertainty on the age of these events, we generate synthetic earthquake sequences by sampling the age of each event within a uniform PDF defined by the minimum and maximum age bounds (following Ellsworth et al. 1999, see Nemer 2023). For each synthetic sequence, a mean interevent time is calculated. We use 1000 synthetic sequences to produce a distribution for the mean interevent time. In Fig. 15, this distribution is superimposed to the rates of ruptures passing through the site, as forecasted by our preferred fault model (M_{max} 7.9, entirely connected). Daeron et al. (2007) evaluated a characteristic coseismic slip of about 5.5m, which according to Leonard (2014) corresponds to an interval of magnitude 7.4 to 8 (extension of the grey box on the graphic). Accounting for the uncertainty on the paleoseismic rates, the observations in the trench are compatible with the forecasts resulting from both the 7.9 and 8.1 maximum magnitude assumptions.

Lefevre et al. (2018) conducted a paleoseismological excavation at the Taybeh site, situated on the Wadi Araba fault, that reveals evidence for twelve surface-rupturing earthquakes spanning the last 8000 years. To build the distribution of mean inter-event times, we use the most complete and reliable part of this earthquake sequence, i.e. the period starting with the 31 BC earthquake that includes 5 earthquakes. To evaluate a magnitude range for these earthquakes, we use the rupture lengths obtained in Lefevre et al. (2018) by correlating the information at different trench sites (grey box in Figure 15). Our fault model forecasts less earthquakes than "observed" at the Taybeh site.

We have compared the forecast to the data observed at two trench sites. A number of other trenches have been excavated along the Levant fault system (e.g. Nemer & Meghraoui 2008, Wechsler et al. 2014, Sbeinati et al. 2010). For a complete evaluation, the forecast should be confronted against observations at all paleoseismic sites available. However, such a comparison is beyond the scope of the present manuscript, it should be considered in future developments of hazard models for the Levant fault system.

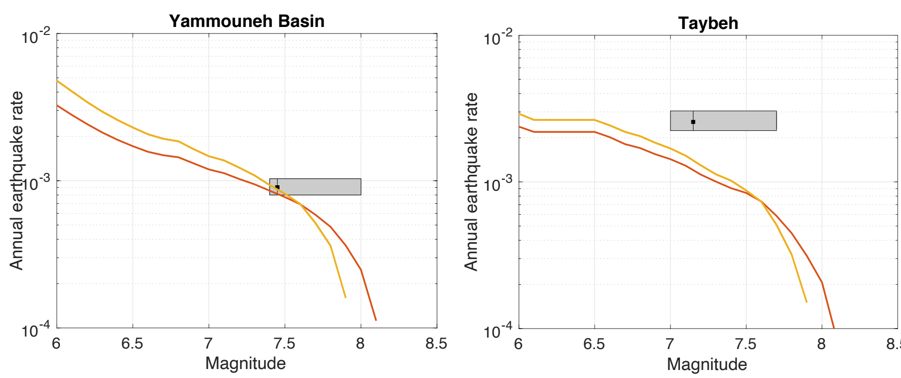

Figure 15: Comparison of the earthquake forecast with rates of earthquakes based on paleoseismic data at two trench sites along the main strand of the LFS. Solid orange line: rates of ruptures passing through the site, as forecasted by the fault model built (also called "participation rates"), a fully interconnected model with M_{max} 7.9 for the Gutenberg-Richter system MFD. Dashed line: fully interconnected model with M_{max} 8.1 for the Gutenberg-Richter system MFD. Rectangle: distribution for the mean inter-event time between large earthquakes, inferred from the paleoseismic data, taking into account the uncertainty on the ages. Left: trench in Yammouneh Basin located along section S40; right: Taybeh trench site on section S8 on Wadi Araba fault (see Fig. 1b and Table 1).

Natural Hazards and Earth System Sciences Discussions

7 Conclusions

The classical way of implementing faults in PSHA, considering separate faults that cannot interact with each other's, is not realistic. In the future, fault models in PSHA must account for complex ruptures, but there is no standard method yet. A few algorithms have been proposed to distribute the moment rate over the physically possible ruptures, SHERIFS (Chartier et al. 2017, 2019) is one of them. This algorithm is being increasingly used (e.g Gomez Novell et al. 2020; Cheng et al. 2021; Moratto et al. 2023, Harrichhausen et al., 2023), however none of the works published up to now analyze the distribution of seismic rates in magnitude and in space that controls hazard levels, nor analyze the results in light of the classical implementation of faults which represents the bulk of PSHA studies at present (both in research and in the industry). The aim of this manuscript is to address these issues.

We test different maximum magnitudes and different shapes for the frequency-magnitude distribution at the fault system level, as summarized in Table 2. We show how the algorithm distributes the seismic rates over the fault system, applying rules for defining which segments can break together. We demonstrate how some key decisions impact the seismic rates, such as the decision on the maximum magnitude the system can produce, or the maximum distance ruptures can jump between segments. The conversion of the slip rates into earthquakes is not straightforward, we display seismic rates maps that help understand the process. Our tests show that the seismic rates associated with a given segment depend strongly on the precise location of the segment within the fault system, and on the segment combinations it can be involved in. Hence, hazard levels are directly related to the implementation of the fault system, its segmentation, and the decision on which segments may break together. In the SHERIFS iterative process, magnitudes are sampled in a PDF at each iteration and associated to a combination of segments (with area matching the magnitude). At the scale of the system, the summed seismic rates follow a Gutenberg-Richter magnitude-frequency distribution (or another MFD shape). However, the set of ruptures and associated rates does not constitute a synthetic catalog (Chartier et al. 2019).

We perform a comparison of a classical fault model implementation with an interconnected fault model, in terms of the distribution in space of seismic rates for different magnitude levels, and in terms of seismic hazard levels. Both models are moment-balanced taking into account fault slip rates. We find that hazard levels may decrease or increase, with respect to the classical implementation, depending on the location of the segment within the system (main strand, secondary strand, segment combinations). For the Levant Fault System, hazard values at a 475 yr return period on average decrease along the main strand (characterized by slip rate of ~4-5 mm/yr), and increase along the secondary faults (characterized by slip rate of the order of ~1-2 mm/yr). One main difference between the models is that the distribution in space of seismic rates is not homogeneous in the interconnected model, even for moderate magnitude earthquakes (M6). These moderate magnitude earthquakes control hazard levels at a 475 yr return period. We find highest hazard levels along segments with the highest seismic rates in the moderate magnitude range.

Among the fault models tested, our preferred model is based on a maximum magnitude 7.9 and a fully interconnected fault system. Five percent of the slip rate is not spent into earthquakes, which is a reasonable amount for aseismic creep along the Levant fault system. Combining this interconnected fault model with a set of ground-motion models valid for the region, hazard levels have been estimated. At a 475 years return period, we find PGA values larger than 0.2g over the entire country of Lebanon; and values larger than 0.3g within 20km of all fault segments considered (rock site conditions). At 0.2s, the spectral accelerations obtained are larger than 0.6g over most of the Lebanon, with highest hazard around 1g for sites on the faults.

https://doi.org/10.5194/nhess-2024-184
Preprint. Discussion started: 2 December 2024

Natural Hazards and Earth System Sciences
Open Access
EGU
Discussions

Table 1 List of the faults, sections, and sub-sections, with corresponding dip, length and width, as well as mean maximum magnitude (inferred from Leonard 2014), and slip rate estimates (see Figure 1). The scaling relationship used is from Leonard 2014.

Fault	Section (tectonic segmentation, see Fig. 1b)	Sub-section (SHERIFS segmentation, see Fig. 1b)	Dip (°)	Length (km)	Width (km)	Mean Slip rate (mm/yr)	Mean maximum magnitude*	
Araba	I	5	90	30.1	18	4.5	6.7	7.5
	II	6		23			6.6	
	III	7		25.8			6.6	
	IV	8		22.9			6.6	
	V	9		10.4			6.0	
	VI	10		18.9			6.5	
	VII	11		22.4			6.6	
		12		21.9			6.6	
	VIII	1		6.5			5.6	
	IX	2		5.3			5.4	
	X	3		4.3			5.3	
	XI	4		25.3			6.6	
Jordan Valley	I	15	90	33.7	18	4.5	6.8	7.5
	II	16		25.2			6.6	
		17		24.4			6.6	
	III	18		27.1			6.7	
	IV	19		13			6.2	
	V	20		28.1			6.7	
		21		28.1			6.7	
Carmel Gilboa	I	46	60	36.5	28	0.5	6.8	6.8
	II	47		16.8			6.4	6.4
Yammouneh	I	13	90	20.2	18	4.5	6.5	7.5
	II	39		35.1			6.8	
		40		34.2			6.8	
	III	41		32.8			6.8	
	IV	42		16.1			6.4	
	V	43		9.5			5.9	
	VI	44		11			6.1	
	VII	45		31.4			6.7	
Rachaya	I	14	90	19.7	18	1.4	6.5	7.1
	II	29		24.8			6.6	
		30		23.8			6.6	
Serghaya	I	36	90	21	18	1.4	6.6	7.2
	II	37		29.1			6.7	
	III	38		39.1			6.8	
Roum	I	31	90	9.9	18	0.9	6.0	7

https://doi.org/10.5194/nhess-2024-184
Preprint. Discussion started: 2 December 2024

Natural Hazards and Earth System Sciences
Open Access
EGU
Discussions

	II	32		7.1			5.7	
	III	33		6			5.5	
	IV	34		6.9			5.7	
	V	35		16			6.4	
Mount Lebanon	I	48	45	20.7	20	1.5	6.6	7.5
	II	49		37.9			6.9	
		50		37			6.9	
	III	51		31.8			6.8	
		52		30.5			6.8	
Missyaf	I	22	90	21.4	18	2.2	6.6	7.3
	II	23		29.7			6.7	
	III	24		32.8			6.8	
		25		32.4			6.7	
Ghab	I	26	90	26	18	2.2	6.7	7
		27		25.9			6.7	
	II	28		27.7			6.7	

*Strike Slip: mean $M_{max} = \log_{10}(A) - 2.0087$ (area A in km^2)
*Reverse: mean $M_{max} = \log_{10}(A) - 2.0013$

Table 2 Different parameterizations tested in the application of the SHERIFS algorithm on the Levant fault system. Seismogenic depth considered: 18km for the strike-slip segments (width of ruptures), 14km for segments on the Mount Lebanon Thrust. GR: Gutenberg Richter, YC: Youngs & Coppersmith. Slip rate increment (dsr) used: 0.0001 mm/yr.

Model	Maximum jump distance	Reccurence model	M_{max}	Length of maximum rupture (km)	Number of rupture combinations	Unused slip rate (%)
1	10	GR	7.5	182	532	9
2	10	GR	7.9	458	3808	64
3	12	GR	7.9	460	8452	21
4	18	GR	7.9	464	18864	5
5	18	GR	8.1	732	119327	11
6	18	YC	7.9	464	18864	14

Code and data availability

The python code used in this study was the version 1.3 from SHERIFS algorithm downloaded from the following website:
https://github.com/tomchartier/SHERIFS (Last time accessed september 2024)

Author contribution

SEK, CB, MB, and YK designed the experiments and SEK carried them out. SEK and CB prepared the manuscript with contributions from all co-authors.

Competing interests

The authors declare that they have no conflict of interest.

Acknowledgements

This research benefited from the support of both the laboratory ISTerre, part of Labex OSUG@2020 (ANR10 LABX56) in France, and the National Center of Geophysics in Lebanon. S. El Kadri benefitted from a SAFAR PhD scholarship financed by the French Embassy in Beirut and the Lebanese CNRS. Her stays in France were also supported by IRD through the ARTS PhD program. We are grateful to Francesco Visini and Martin Mai who read an earlier version of the manuscript and provided very useful feedbacks. We are also grateful to Océane Foix for her kind help in displaying some of the maps. At last, we would like to warmly thank Nicolas Harrichhausen for the fruitful discussions regarding SHERIFS implementation and for a careful prooreading of the manuscript.

References

Akkar, S., M. A. Sandikkaya, and J. J. Bommer (2014). Empirical ground-motion models for point- and extended-source crustal earthquake scenarios in Europe and the Middle East, Bull. Earthq. Eng. 12, no. 1, 359–387. https://doi.org/10.1007/s10518-013-9461-4

Ambraseys, N. N., and Jackson, J. A. (1998). Faulting associated with historical and recent earthquakes in the Eastern Mediterranean region. Geophysical Journal International, 133(2), 390-406.

al Tarazi, E., J. Abu Rajab, F. Gomez, W. Cochran, R. Jaafar, and M. Ferry (2011), GPS measurements of near-field deformation along the southern Dead Sea Fault System, Geochem. Geophys. Geosyst., 12, Q12021, doi:10.1029/2011GC003736

Brax M, Albini P, Beauval C, Jomaa R, Sursock A (2019) An earthquake catalog for the Lebanese region. Seismol Res Lett 90(6):2236-2249. https://doi.org/10.1785/0220180292

Chartier, T., Scotti, O., Lyon-Caen, H., & Boiselet, A. (2017). Methodology for earthquake rupture rate estimates of fault networks: Example for the western Corinth rift, Greece. *Natural Hazards and Earth System Sciences,17*(10), 1857–1869. https://doi.org/10.5194/nhess-17-1857-2017.

Chartier T, Scotti O, Lyon-Caen H. (2019). SHERIFS: Open-source code for computing earthquake rates in fault systems and constructing hazard models. Seismol Res Lett, 90: 1678–1688

Cheng, J., Xu, X., Ren, J., Zhang, S., & Wu, X. (2021). Probabilistic multi-segment rupture seismic hazard along the Xiaojiang fault zone, southeastern Tibetan Plateau. *Journal of Asian Earth Sciences*, *221*, 104940

Chiou, B. S. J., and Youngs, R. R. (2014). Update of the Chiou and Youngs NGA model for the average horizontal component of peak ground motion and response spectra. Earthquake Spectra, 30(3), 1117-1153.

Daeron M, Benedetti L, Tapponnier P, Sursock A, Finkel RC (2004) Constraints on the post~ 25-ka slip rate of the Yammouneh fault (Lebanon) using in situ cosmogenic 36Cl dating of offset limestone clast fans. Earth Planet Sci Lett 227(1–2):105–119. https://doi.org/10.1016/j.epsl.2004.07.014

Daëron, M. (2005), Rôle, cinématique et comportement sismique à long terme de la faille de Yammouneh, Thèse de doctorat, 178 pp., Inst. De Phys. du Globe de Paris, Paris.

Daeron M, Klinger Y, Tapponnier P, Elias A, Jacques E, Sursock A (2005) Sources of the large AD 1202 and 1759 Near East earthquakes. Geology 33(7):529–532. https://doi.org/10.1130/G21352.1

Daeron M, Klinger Y, Tapponnier P, Elias A, Jacques E, Sursock A (2007) 12,000-year-long record of 10 to 13 paleoearthquakes on the Yammouneh fault, Levant fault system, Lebanon. Bull Seismol Soc Am 97(3):749–771. https://doi.org/10.1785/0120060106

Danciu, L., Giardini, D., Weatherill, G., Basili, R., Nandan, S., Rovida, A., Beauval, C., Bard, P.-Y., Pagani, M., Reyes, C. G., Sesetyan, K., Vilanova, S., Cotton, F., and Wiemer, S. (2024): The 2020 European Seismic Hazard Model: Overview and Results, in press in NHESS, https://doi.org/10.5194/egusphere-2023-3062

Eberhart-Phillips, D., P. J. Haeussler, J. T. Freymueller, A. D. Franckel, C. M. Rubin, P. Craw, N. A. Ratchkovski, G. Anderson, G. A. Carver, A. J. Crone, T. E. Dawsson, H. Fletcher, R. Hansen, E. L. Harp, R. A. Harris, D. P. Hill, S. Hreinsdottiir, R. W. Jibson, L. M. Jones, R. Kayen, D. K. Keefer, C. F. Larsen, S. C. Moran, S. F. Personius, G. Plafker, B. Sherrod, K. Sieh, N. Sitar, and W. K. Wallace (2003). The 2002 Denali fault earthquake, Alaska: a large magnitude, slip-partitioned event, Science 300, 1113–1118.

Elias, A., P. Tapponnier, S. C. Singh, G. C. P. King, A. Briais, M. Daëron, H. Carton, A. Sursock, E. Jacques, R. Jomaa, and Y. Klinger (2007), Active thrusting offshore Mount Lebanon: Source of the tsunamigenic A.D. 551 Beirut-Tripoli earthquake, *Geology*, 35, 755–758, doi:710.1130/G2363A.

El Kadri, S., Beauval, C., Brax, M., Bard, P. Y., Vergnolle, M., & Klinger, Y. (2023). A fault-based probabilistic seismic hazard model for Lebanon, controlling parameters and hazard levels. *Bulletin of Earthquake Engineering*, *21*(7), 3163-3197.https://doi.org/10.1007/s10518-023-01631-z

Ekström, G., Nettles, M., & Dziewoński, A. M. (2012). The global CMT project 2004–2010: Centroid-moment tensors for 13,017 earthquakes. Physics of the Earth and Planetary Interiors, 200, 1-9.

Ellsworth, W. L., Matthews, M. V., Nadeau, R. M., Nishenko, S. P., Reasenberg, P. A., & Simpson, R. A. (1999). A physically-based earthquake recurrence model for estimation of long-term earthquake probabilities. Workshop on earthquake recurrence: state of the art and directions for the future, Istituto Nazionale de Geofisica, Rome, Italy, 22-25 February, 1999, proceeding, 22pp.

Ferry M, Meghraoui M, Abou Karaki N, Al-Taj M, Khalil L (2011) Episodic behavior of the Jordan Valley section of the Dead Sea fault inferred from a 14-ka-long integrated catalog of large earthquakesepisodic behavior of the Jordan Valley section of the Dead Sea fault. Bull Seismol Soc Am101(1):39–67. https://doi.org/10.1785/0120100097

Field, E. H., Arrowsmith, R. J., Biasi, G. P., Bird, P., Dawson, T. E., Felzer, K. R., Jackson, D. D., Johnson, K. M., Jordan, T. H., Madden, C., Michael, A. J., Milner, K. R., Page, M. T., Parsons, T., Powers, P. M., Shaw, B. E., Thatcher, W. R., Weldon, R. J., Zeng, Y., (2014). Uniform California earthquake rupture forecast, version 3 (UCERF3)—The time-independent model. *Bulletin of the Seismological Society of America*, *104*(3), 1122-1180. doi: https://doi.org/10.1785/0120130164

Fletcher, J., Teran, O. J., Rockwell, T. K., Oskin, M. E., Hudnut, K. W., Mueller, K. J., et al. (2014). Assembly of a large earthquake from a complex fault system: Surface rupture kinematics of the 4 April 2010 El Mayor-Cucapah (Mexico) M_w 7.2 earthquake. *Geosphere*, 10, 797–827. https://doi.org/10.1130/ges00933.1

Geist, E. L., & ten Brink, U. S. (2021). Earthquake magnitude distributions on northern Caribbean faults from combinatorial optimization models. *Journal of Geophysical Research: Solid Earth*, *126*(10), e2021JB022050.

Gomez, F., M. Meghraoui, A. N. Darkal, F. Hijazi, M. Mouty, Y. Suleiman,R. Sbeinati, R. Darawcheh, R. Al-Ghazzi, and M. Barazangi (2003),Holocene faulting and earthquake recurrence along the Serghaya branchof the Dead Sea fault system in Syria and Lebanon,Geophys. J. Int.,153,658–674, https://doi.org/10.1046/j.1365-246X.2003.01933.x

https://doi.org/10.5194/nhess-2024-184
Preprint. Discussion started: 2 December 2024

Gomez, F., G. Karam, M. Khawlie, S. McClusky, P. Vernant, R. Reilinger, R. Jaafar, C. Tabet, K. Khair, and M. Barazangi (2007a), Global Positioning System measurements of strain accumulation and slip transfer through the restraining bend along the Dead Sea fault system in Lebanon, *Geophys. J. Int.*, 168(3), 1021–1028, doi:10.1111/j.1365-246X.2006.03328.x.

Gomez, F., Nemer, T., Tabet, C., Khawlie, M., Meghraoui, M., & Barazangi, M. (2007b). Strain partitioning of active transpression within the Lebanese restraining bend of the Dead Sea Fault (Lebanon and SW Syria). *Geological Society, London, Special Publications*, *290*(1), 285-303.

Gómez-Novell O, García-Mayordomo J, Ortuño M, Masana E and Chartier T (2020) Fault System-Based Probabilistic Seismic Hazard Assessment of a Moderate Seismicity Region: The Eastern Betics Shear Zone (SE Spain). Front. Earth Sci. 8:579398. doi: 10.3389/feart.2020.579398

Gupta, A., & Scholz, C. H. (2000). A model of normal fault interaction based on observations and theory. Journal of structural Geology, 22(7), 865-879.

Hamling, I. J., Hreinsdóttir, S., Clark, K., Elliott, J., Liang, C., Fielding, E., Litchfield N., Villamor P., Wallace L., Wright T.J., D'Anastasio E., Bannister S., Burbridge D., Denys P., Gentle P., Howarth J., Mueller C., Palmer N., Pearson C., Power W., Barnes P., Barrell D., Van Dissen R., Langridge R., Little T., Nicol A., Pettinga J., Rowland J. & Stirling, M. (2017). Complex multifault rupture during the 2016 M w 7.8 Kaikōura earthquake, New Zealand. Science, 356(6334), eaam7194.

Harrichhausen, N., Audin, L., Baize, S., Johnson, K. L., Beauval, C., Jarrin, P., Marconato, L., Rolandone, F., Jomard, H., Nocquet, J.-M., Alvarado, A., Mothes, P.A. (2024). Fault source models show slip rates measured across the width of the entire fault zone best represent the observed seismicity of the Pallatanga–Puna Fault, Ecuador. Seismological Research Letters, 95(1), 95-112.

Harris, R. A., & Day, S. M. (1993). Dynamics of fault interaction: Parallel strike-slip faults. Journal of Geophysical Research: Solid Earth, 98(B3), 4461-4472.

Klinger, Y., Xu, X., Tapponnier, P., Van der Woerd, J., Lasserre, C., & King, G. (2005). High-resolution satellite imagery mapping of the surface rupture and slip distribution of the M w∼ 7.8, 14 November 2001 Kokoxili earthquake, Kunlun fault, northern Tibet, China. Bulletin of the Seismological Society of America, 95(5), 1970-1987.

Klinger, Y., Le Béon, M., & Al-Qaryouti, M. (2015). 5000 yr of paleoseismicity along the southern Dead Sea fault. *Geophysical Journal International*, *202*(1), 313-327.

Klinger, Y., Okubo, K., Vallage, A., Champenois, J., Delorme, A., Rougier, E., Lei, Z., Knight, E. E., Munjiza, A., Satriano, C., Baize, S., Langridge, R., & Bhat, H. S. (2018). Earthquake damage patterns resolve complex rupture processes. *Geophysical Research Letters*, 45, 10,279–210,287. https://doi.org/10.1029/2018GL078842

Kotha SR, Weatherill G, Bindi D, Cotton F (2020) A regionally-adaptable ground-motion model for shallow crustal earthquakes in Europe. Bull Earthq Eng 18(9):4091–4125. https://doi.org/10.1007/s10518-020-00869-1

Lefevre, M., Klinger, Y., Al-Qaryouti, M., Le Béon, M., & Moumani, K. (2018). Slip deficit and temporal clustering along the Dead Sea fault from paleoseismological investigations. *Scientific reports*, *8*(1), 4511.

Leonard M (2014) Self-consistent earthquake fault-scaling relations: update and extension to stable continental strike-slip faults. Bull Seismol Soc Am 104(6):2953–2965. https://doi.org/10.1785/0120140087

Lolli, B., P. Gasperini, and G. Vannucci (2014). Empirical conversion between teleseismic magnitudes (mb and Ms) and moment magnitude (Mw) at the Global, Euro-Mediterranean and Italian scale, Geophys. J. Int. 199, 805–828.

Lu, Y., Wetzler, N., Waldmann, N., Agnon, A., Biasi, G. P., & Marco, S. (2020). A 220,000-year-long continuous large earthquake record on a slow-slipping plate boundary. Science Advances, 6(48), eaba4170.

Meghraoui M, Gomez F, Sbeinati R et al. (2003) Evidence for 830 years of seismic quiescence from palaeoseismology, archaeoseismology and historical seismicity along the Dead Sea fault in Syria. Earth Planet Sci Lett 210(1–2):35–52. https://doi.org/10.1016/S0012-821X(03)00144-4

Meghraoui, M. (2015). Paleoseismic history of the Dead Sea fault zone, In: Beer, M., Kougioumtzoglou, I., Patelli, E., Au, IK. (eds) Encyclopedia of Earthquake Engineering. Springer, Berlin, Heidelberg. https://doi.org/10.1007/978-3-642-36197-5_40-1

Meletti C, Marzocchi W, D'Amico V, Lanzano G, Luzi L, Martinelli F, Pace B, Rovida A, Taroni M, Visini F (2021) The new Italian seismic hazard model (MPS19). Ann Geophys 64(1):SE112. https://doi.org/10.4401/ag-8579

Moratto, L., Santulin, M., Tamaro, A., Saraò, A., Vuan, A., & Rebez, A. (2023). Near-source ground motion estimation for assessing the seismic hazard of critical facilities in central Italy. Bulletin of Earthquake Engineering, 21(1), 53-75, https://doi.org/10.1007/s10518-022-01555-0.

Nemer, B. (2023). Time-dependent models for on-fault earthquakes in a PSHA study, Grenoble Alp University, Master in Natural Hazards in Civil Engineerings, internship report, 31p.

Nemer T, Meghraoui M (2006) Evidence of coseismic ruptures along the Roum fault (Lebanon): a possible source for the AD 1837 earthquake. J Struct Geol 28(8):1483–1495. https://doi.org/10.1016/j.jsg.2006.03.038

Nemer T, Meghraoui M, Khair K (2008) The Rachaya-Serghaya fault system (Lebanon): evidence of coseismic ruptures, and the AD 1759 earthquake sequence. J Geophys Res: Solid Earth 113(5):1–12. https://doi.org/10.1029/2007JB005090

Nemer, T., Gomez, F., Al Haddad, S., & Tabet, C. (2008). Coseismic growth of sedimentary basins along the Yammouneh strike-slip fault (Lebanon). Geophysical Journal International, 175(3), 1023–1039. https://doi.org/10.1111/j.1365-246X.2008.03889.x

Pagani M, Monelli D, Weatherill G et al. (2014) OpenQuake-engine: an open hazard (and risk) software for the global earthquake model. Seismol Res Lett 85(3):692–702. https:// doi. org/ 10. 1785/ 0220130087

Page, M. T., Field, E. H., Milner, K. R., & Powers, P. M. (2014). The UCERF3 grand inversion: Solving for the long-term rate of ruptures in a fault system. *Bulletin of the Seismological Society of America*, *104*(3), 1181-1204.

Sbeinati MR, Meghraoui M, Suleyman G, Gomez F, Grootes P, Nadeau M, Al Najjar H, Al-Ghazzi R (2010) Timing of earthquake ruptures at the Al Harif Roman Aqueduct (Dead Sea fault, Syria) from archeoseismology and paleoseismology, Special volume "Archaeoseismology and paleoseismology. In: Sintubin M, Stewart IS, Niemi TM, Altunel E (eds) Ancient earthquakes: geological society of America special paper, 471. doi:10.1130/2010.2471(20)

Scholz, C. H., & Gupta, A. (2000). Fault interactions and seismic hazard. *Journal of Geodynamics*, *29*(3-5), 459-467.

Sesetyan, K., Demircioglu, M. B., Duman, T. Y., Çan, T., Tekin, S., Azak, T. E., & Fercan, Ö. Z. (2018). A probabilistic seismic hazard assessment for the Turkish territory—part I: the area source model. *Bulletin of Earthquake Engineering*, *16*, 3367-3397.

Storchak, D. A., D. Di Giacomo, E. R. Engdahl, J. Harris, I. Bondár, W. H. K. Lee, P. Bormann, and A. Villaseñor (2015). The ISC-GEM Global Instrumental Earthquake Catalog (1900–2009): Introduction, Phys. Earth Planet. In. 239, 48–63, doi:10.1016/j.pepi.2014.06.009.

Storchak, D. A., Harris, J., Brown, L., Lieser, K., Shumba, B., & Di Giacomo, D. (2020). Rebuild of the Bulletin of the International Seismological Centre (ISC)—part 2: 1980–2010. *Geoscience Letters*, *7*(1), 1-21.

Visini, F., Valentini, A., Chartier, T., Scotti, O., & Pace, B. (2020). Computational tools for relaxing the fault segmentation in probabilistic seismic hazard modelling in complex fault systems. *Pure and Applied Geophysics*, *177*, 1855-1877.

Wang, Y. J., Chan, C. H., Lee, Y. T., Ma, K. F., Shyu, J. B. H., Rau, R. J., & Cheng, C. T. (2016). Probabilistic seismic hazard assessment for Taiwan. *Terr. Atmos. Ocean. Sci*, *27*(3), 325-340.

Wechsler N, Rockwell TK, Klinger Y, Štěpančíková P, Kanari M, Marco S, Agnon A (2014) A paleoseismic record of earthquakes for the Dead Sea transform fault between the first and seventh centuries CE: nonperiodic behavior of a plate boundary fault. Bull Seismol Soc Am 104(3):1329–1347. https:// doi.org/ 10. 1785/ 01201 30304

Wechsler, N., Rockwell, T. K., & Klinger, Y. (2018). Variable slip-rate and slip-per-event on a plate boundary fault: The Dead Sea fault in northern Israel. *Tectonophysics*, *722*, 210-226.

Wesnousky, S. G. (2006). Predicting the endpoints of earthquake ruptures. *Nature*, *444*(7117), 358-360.

Yeats, R. S.; Sieh, K. E.; Allen, C. R. 1997: The geology of earthquakes. New York, Oxford University Press. 568 p.

Youngs, R. R., & Coppersmith, K. J. (1985). Implications of fault slip rates and earthquake recurrence models to probabilistic seismic hazard estimates. *Bulletin of the Seismological society of America*, *75*(4), 939-964.

Zare M, Amini H, Yazdi P, Sesetyan K, Demircioglu MB, Kalafat D, Erdik M, Giardini D, Khan MA, Tsereteli N (2014) Recent developments of the Middle East catalog. *Journal of Seismology* 18: 749–772.

Zhang, Y., Tang, X., Liu, D., Taymaz, T., Eken, T., Guo, R., Zheng, Y., Wang, J., and Sun, H (2023). Geometric controls on cascading rupture of the 2023 Kahramanmaraş earthquake doublet. Nature Geoscience, doi:10.1038/s41561-023-01283-3